nature nanotechnology

Article

https://doi.org/10.1038/s41565-024-01815-x

Self-cleaning electrode for stable synthesis of alkaline-earth metal peroxides

Received: 17 April 2024

Accepted: 27 September 2024

Published online: 28 October 2024

Check for updates

Minli Wang[1,2,4], Jinhuan Cheng[3,4], Wenwen Xu[1,2] ✉, Dandan Zhu[3], Wuyong Zhang[1], Yingjie Wen[1], Wanbing Guan[1,2], Jinping Jia[3] ✉ & Zhiyi Lu[1,2] ✉

Alkaline-earth metal peroxides (MO_2, M = Ca, Sr, Ba) represent a category of versatile and clean solid oxidizers, while the synthesis process usually consumes excessive hydrogen peroxide (H_2O_2). Here we discover that H_2O_2 synthesized via two-electron electrochemical oxygen reduction ($2e^-$ ORR) on the electrode surface can be efficiently and durably consumed to produce high-purity MO_2 in an alkaline environment. The crucial factor lies in the in-time detachment of in situ-generated MO_2 from the self-cleaning electrode, where the solid products spontaneously detach from the electrode to solve the block issue. The self-cleaning electrode is achieved by constructing micro-/nanostructure of a highly active catalyst with appropriate surface modification. In experiments, an unprecedented accumulated selectivity (~99%) and durability (>1,000 h, 50 mA cm^{-2}) are achieved for electrochemical synthesis of MO_2. Moreover, the comparability of CaO_2 and H_2O_2 for tetracycline degradation with hydrodynamic cavitation is validated in terms of their close efficacies (degradation efficiency of 87.9% and 93.6% for H_2O_2 and CaO_2, respectively).

Alkaline-earth metal peroxides (MO_2, M = Ca, Sr, Ba), featuring strong oxidability and relatively stable chemical property compared with hydrogen peroxide (H_2O_2), have been worldwidely utilized in the fields of bleaching, wastewater treatment, disinfection and chemical synthesis[1–5]. For example, the application of CaO_2 in the field of water treatment has been extensively researched and studied[6,7]. The current synthesis of MO_2 mainly involves the mixing of alkaline-earth metal oxides or hydroxides with highly concentrated H_2O_2 (10–30 wt%)[8–11], as schemed in Fig. 1a. However, the H_2O_2 with a concentration over 8 wt% belongs to explosive chemicals, which strictly restricts its long-distance transportation and mass storage[12–16]. More critically, during the chemical synthesis of MO_2, the alkaline environment triggers fast decomposition of H_2O_2 (ref. 17), resulting in insufficient utilization of H_2O_2 (Supplementary Figs. 1 and 2 and Supplementary Table 1).

To circumvent the explosion risk arising from H_2O_2 transportation and storage, the researchers have adopted a two-electron electrochemical oxygen reduction ($2e^-$ ORR) pathway to generate and accumulate H_2O_2, which is subsequently used for chemical synthesis of MO_2 (ref. 18), as schemed in Fig. 1b. Although encouraging accomplishments on catalysts for selective $2e^-$ ORR reaction have been achieved recently[19–22], the inevitable self-decomposition of H_2O_2 during the accumulation process gives rise to unsatisfactory Faradaic efficiency (FE). Meanwhile, the fast decomposition issue of H_2O_2 in the sequential chemical synthesis of MO_2 is still remaining.

Aiming at simultaneous improvement of the FE and utilization rate of H_2O_2, we propose an in situ electrochemical synthesis strategy, where the generated H_2O_2 instantaneously reacts with M^{2+} dwelling in electrolyte to produce MO_2 on the electrode surface, as schemed in Fig. 1c,d. This method has two obvious advantages: (i) the existed M^{2+} enables the immediate consumption of as-generated HO_2^- on the electrode surface, thus avoiding the self-decomposition of H_2O_2 and improving the accumulated FE for the $2e^-$ ORR process; (ii) the electrode surface

[1]Key Laboratory of Marine Materials and Related Technologies, Zhejiang Key Laboratory of Advanced Fuel Cells and Electrolyzers Technology, Ningbo Institute of Materials Technology and Engineering, Chinese Academy of Sciences, Ningbo, China. [2]School of Chemical Sciences, University of Chinese Academy of Sciences, Beijing, China. [3]School of Environmental Science and Engineering, Shanghai Jiaotong University, Shanghai, China. [4]These authors contributed equally: Minli Wang, Jinhuan Cheng. ✉e-mail: xuwenwen@nimte.ac.cn; jpjia@sjtu.edu.cn; luzhiyi@nimte.ac.cn

https://doi.org/10.1038/s41565-024-01815-x

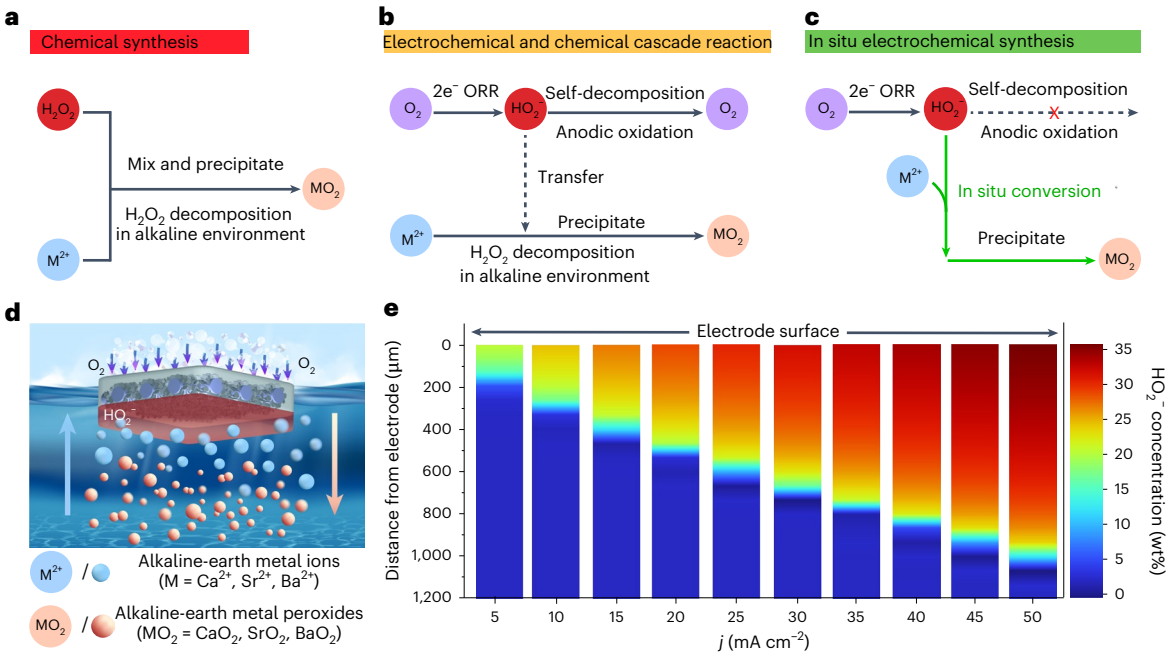

Fig. 1 | Schematic illustrations of the synthesis process of MO_2. a–d, Chemical synthesis process of MO_2 (**a**), electrochemical and chemical cascade synthesis process of MO_2 (**b**) and in situ electrochemical synthesis process of MO_2 with self-cleaning electrode (**c**,**d**). **e**, The COMSOL simulated concentration profiles of H_2O_2 after 5 s reaction at current densities ranging from 5 mA cm^{-2} to 50 mA cm^{-2}.

will be surrounded with highly concentrated HO_2^- (up to 30 wt% within 600 μm from the electrode at 50 mA cm^{-2}, as simulated in Fig. 1e), which is favourable to trigger the formation of MO_2. The corresponding experimental results also convinced the higher concentration of H_2O_2 near the surface (Supplementary Figs. 3–6). However, during the synthetic process, the solid MO_2 product tends to severely adhere on the electrode surface (for example, scaling effect) owing to the strong solid–solid adhesion, resulting in a fast decrease of active area and performance degradation[23].

In this work, we discover that the scaling effect during in situ electrochemical synthesis of MO_2 is highly dependent on the adhesion of the electrode surface towards the electrolyte. The low adhesive surface greatly reduces the solid–liquid contact area, resulting in decreased nucleation sites and in-time detachment for solid product (that is, self-cleaning effect). As a proof of concept, a micro-/nanostructured Ni-doped oxygenated carbon electrode with Teflon coating (T-NiOC) is constructed and utilized for MO_2 synthesis. The NiOC catalyst has been demonstrated to be effective in the selective 2e⁻ ORR process[24], and herein the ultra-low surface adhesion that is realized by the combination of micro-/nanostructure and low surface energy polymer modification dominantly contributes to the rapid MO_2 detachment from the electrode surface. As a result, the lab-made system assembled by T-NiOC cathode and conventional anode (dimensionally stable anode, denoted as DSA) achieves an outstanding accumulated FE of ~99% and stability over 1,000 h for the synthesis of SrO_2, while severe scaling problem and fast current degradation within 60 h is observed on the electrode with higher surface adhesion (NiOC/TCFP). In virtue of the self-cleaning electrode, this electrochemical synthesis strategy is generally applicable to other representative MO_2, including CaO_2 and BaO_2. Moreover, the potential application of MO_2 product for wastewater treatment is demonstrated by the hydrodynamic cavitation (HC) method.

Results

Figure 2a illustrates the lab-made system for in situ electrochemical synthesis of MO_2, where the cathode utilized for MO_2 synthesis is floating in the interface between electrolyte and oxygen atmosphere. This working state of the cathode could simultaneously accelerate the oxygen diffusion to the reaction site and detachment of MO_2 from the electrode. To maximize the conversion efficiency, the electrolyte should continuously flow as M^{2+} is constantly consumed and need to be replenished to maintain a saturated concentration of M^{2+} (Supplementary Fig. 7). Take the example of SrO_2 synthesis; the typical ORR polarization curves of the T-NiOC electrode, NiOC electrode without Teflon coating (NiOC) and powdery NiOC catalyst drop-casted on Teflon-coated carbon fibre paper (NiOC/TCFP) in 0.4 M NaOH + saturated $Sr(OH)_2$ electrolyte are shown in Fig. 2b. It could be observed that the T-NiOC electrode demonstrated a current density exceeding 100 mA cm^{-2} at 0.2 V versus RHE, while the NiOC electrode possessed a distinctly attenuated current density (<5 mA cm^{-2}), indicating the crucial role of surface energy modulation in gas diffusion[25–27] (Supplementary Figs. 8 and 9). The red line in Fig. 2b showed that the NiOC/TCFP electrode exhibited slightly compromised ORR performance, which could be attributed to the absence of micro-/nanostructure[28–30] (Supplementary Fig. 10). In addition, the absence of $Sr(OH)_2$ in the electrolyte did not affect the catalytic ORR activity of the T-NiOC electrode (blue line in Fig. 2b).

The stability and selectivity are two paramount important parameters for evaluating the application potential of this in situ synthesis of MO_2. For the stability, the T-NiOC electrode exhibited an exceptional durability for over 1,000 h at a current density of 50 mA cm^{-2}, whereas the NiOC/TCFP electrode experienced a rapid voltage increase and subsequent deactivation within 60 h (Fig. 2c and Supplementary Figs. 11 and 12). The primary factor was the occurrence of apparent adhesion of solid product on the electrode surface, which severely blocked the active sites for 2e⁻ ORR. Nevertheless, an exceptional self-cleaning phenomenon was observed on the T-NiOC electrode, as evidenced by optical and scanning electron microscopy (SEM) (Supplementary Fig. 13). As to the selectivity, the T-NiOC electrode maintained a high accumulated FE ranging from 97.9% to 98.9% within a time frame of 6–24 h in the electrolyte with 0.4 M NaOH and saturated $Sr(OH)_2$, while the FE drastically dropped to 73.1–40.3% in the electrolyte without $Sr(OH)_2$ owing to the highly self-decomposition rate of the accumulated H_2O_2 (Fig. 2d and Supplementary Figs. 14 and 15). This remarkable enhancement of accumulated FE in terms of active O_2^{2-} can be

https://doi.org/10.1038/s41565-024-01815-x

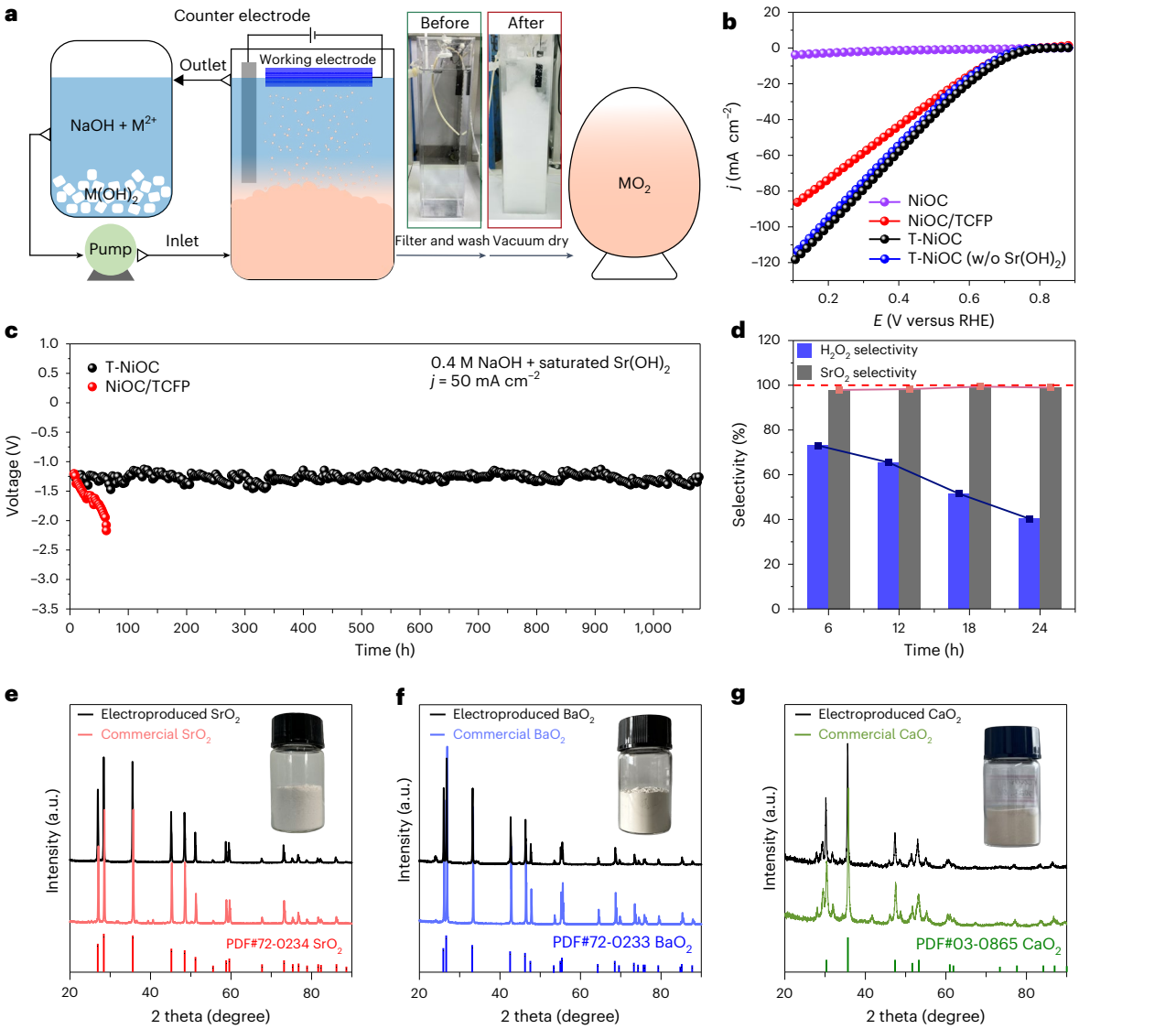

Fig. 2 | The performance of in situ electrochemical synthesis of MO_2. **a**, Scheme of the in situ electrochemical synthesis system for MO_2. **b**, ORR polarization curves of NiOC, T-NiOC and NiOC/TCFP electrodes in an alkaline environment with and without $Sr(OH)_2$, respectively. **c**, The corresponding stability of T-NiOC and NiOC/TCFP electrode in 0.4 M NaOH + saturated $Sr(OH)_2$ with a current density of 50 mA cm^{-2}. **d**, Accumulated FE comparison of H_2O_2 and SrO_2 as the target products. The red dashed line represents the position with 100% selectivity. **e**–**g**, XRD patterns and optical images of collected SrO_2 (**e**), BaO_2 (**f**) and CaO_2 (**g**) products by the in situ electrochemical synthesis method.

attributed to the timely conversion of H_2O_2 into SrO_2 and the excellent chemical stability of SrO_2, thereby preventing the decomposition of H_2O_2 in anodic oxidation and alkaline environments. It should be pointed out that the reaction current density needs to be optimized. Insufficient involvement of Sr^{2+} in the reaction compromises the FE at high current densities, while a low current density fails to meet the demands for large-scale synthesis of SrO_2 (Supplementary Fig. 16).

It is worth noting that the solid SrO_2 produced by our in situ electrochemical synthesis strategy exhibited a purity of 93%, as confirmed by the X-ray powder diffractometer (XRD) patterns and thermogravimetric analysis (TGA) (Fig. 2e and Supplementary Figs. 17 and 18). Moreover, this synthetic strategy is generally applicable towards BaO_2 and CaO_2. For the synthesis of BaO_2, the high solubility of raw $Ba(OH)_2$ ensures sufficient concentration of Ba^{2+} in the electrolyte for the in situ conversion of O_2^{2-}, resulting in an accumulated FE of ~99% at a current density of 50 mA cm^{-2}. The purity of BaO_2 exceeded 98%, while the additional peaks observed in the XRD pattern primarily were arisen from the presence of $BaCO_3$, which was inherent to the raw material (Fig. 2f and Supplementary Figs. 19–21). For the synthesis of CaO_2, the limited solubility of $Ca(OH)_2$ greatly affected the reaction rate; thus, the given current density was adjusted to 5 mA cm^{-2} with a slightly decreased FE of ~70%. The synthesized CaO_2 exhibited an XRD pattern that was identical to that of the commercial CaO_2, and its purity reached a remarkable level of 98.3% as confirmed by TGA (Fig. 2e and Supplementary Figs. 22 and 23). Therefore, the exceptional stability, satisfied accumulated FE and high purity of products demonstrated great potential of the in situ electrochemical synthesis technique for practical applications.

To further visualize and clarify the self-cleaning process and surface state of the electrodes (T-NiOC and NiOC/TCFP), we conducted the in situ and ex situ observations outside the electrode surface using a high-speed camera (Supplementary Fig. 24) and 3D optical profilometer, respectively. As shown in Fig. 3a, the 'needle-like' SrO_2 was in situ generated on the T-NiOC electrode surface within 5 min, characterized by a limited contact area with the electrode surface. Within 13 min, the 'SrO_2 jungle' gradually grew with reaction proceeds, and

https://doi.org/10.1038/s41565-024-01815-x

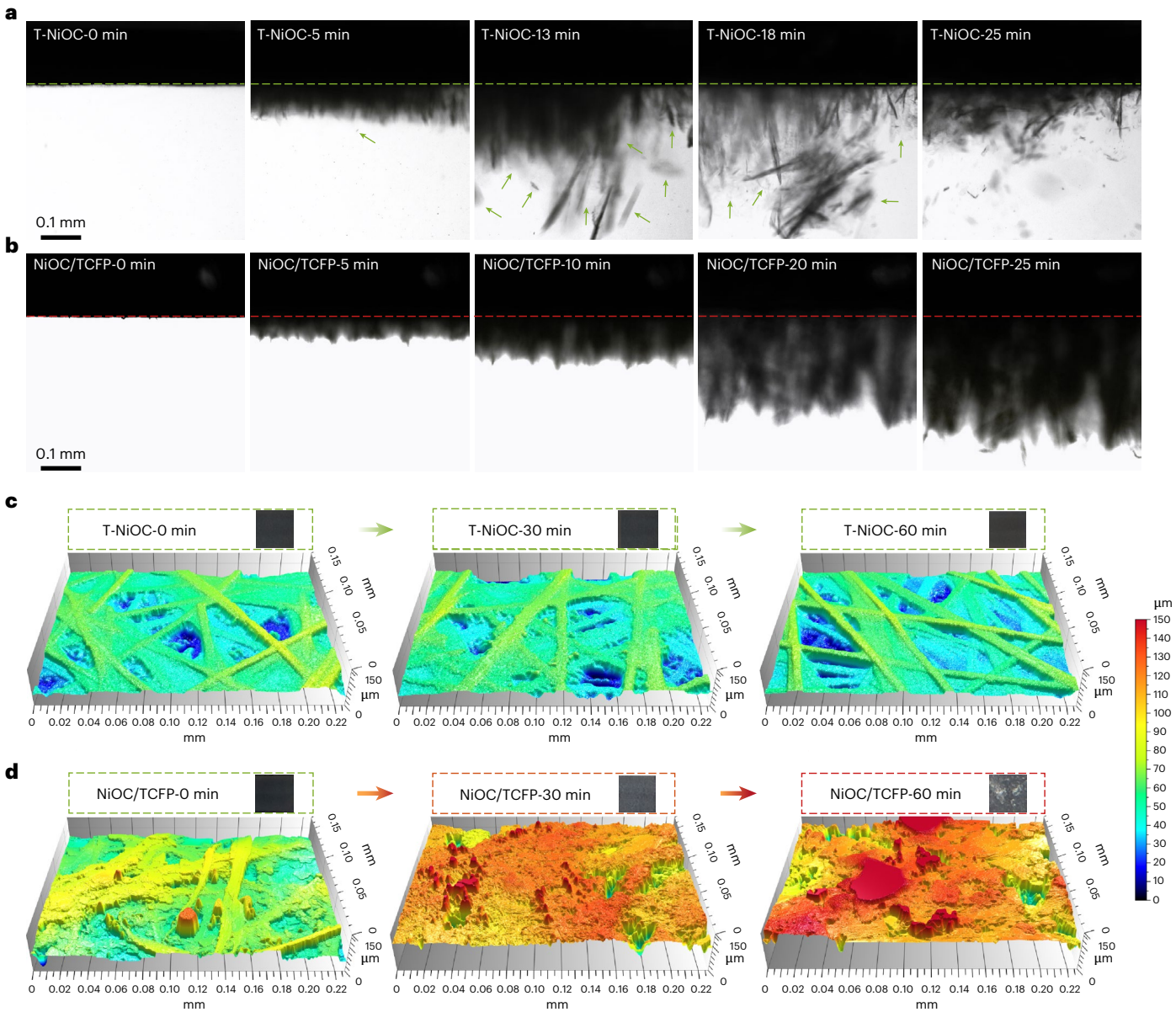

Fig. 3 | Self-cleaning process of the T-NiOC electrode. a,**b**, Photographs of the in situ electrochemical synthesis of SrO_2 on the T-NiOC (**a**) and NiOC/TCFP (**b**) electrode surface in 0.4 M NaOH + 0.0576 M $Sr(OH)_2$ solution recorded by a high-speed camera. The green and red dashed lines represent the bottom boundaries of the T-NiOC and NiOC/TCFP electrodes, respectively. The green arrows point to SrO_2 solid products detached from the electrode surface. **c**,**d**, 3D optical profiler photographs of the reacted T-NiOC (**c**) and NiOC/TCFP (**d**) electrodes.

simultaneously part of the SrO_2 product automatically detached from the electrode surface. After that, the behaviour of the SrO_2 product was dominated by detachment rather than adhesion to the electrode surface. Notably, negligible accumulation of SrO_2 was observed on the T-NiOC surface even after 50 min of reaction (Supplementary Fig. 25); instead, the electrolyte was filled with a large amount of the free SrO_2 product. In sharp contrast, the solid products continuously accumulated on the surface of the NiOC/TCFP electrode as the reaction progressed, eventually covering the electrode surface completely (Fig. 3b and Supplementary Figs. 26 and 27). The corresponding ex situ 3D optical profile photos also confirmed the difference in the self-cleaning ability of the two electrodes. As shown in Fig. 3c, the carbon fibre structure maintained clean without observable fluctuation in height, indicating the absence of adhered products to the T-NiOC electrode surface. As for the NiOC/TCFP electrode, the corresponding 3D optical profile photos (Fig. 3d) revealed a gradual roughening of the surface and an increase in height, indicating the continuous adherence of the SrO_2 products.

Closer inspection on the materials characterizations may shed light on the underlying mechanism for the self-cleaning property of the T-NiOC electrode. As comparison, the NiOC/TCFP electrode, which exhibited a rapid voltage drop during SrO_2 synthesis, could be explained by the severe aggregation of generated inactive SrO_2 on the electrode surface (Fig. 4a and Supplementary Fig. 28). As a result, the liquid contact angle (LCA) of the NiOC/TCFP electrode apparently decreased from 127° to 39.9° after reaction (inset of Fig. 4a). The T-NiOC electrode surface could preserve the surface micro-/nanostructure, resulting in a slight LCA change (163° to 142°; Fig. 4b). Adhesion test results revealed that the T-NiOC electrode showed a low adhesive force to electrolyte (34 μN), whereas the NiOC/TCFP electrode demonstrated a much stronger adhesion (~178 μN), as shown in Fig. 4c. It should be noted that the surface modification of the

https://doi.org/10.1038/s41565-024-01815-x

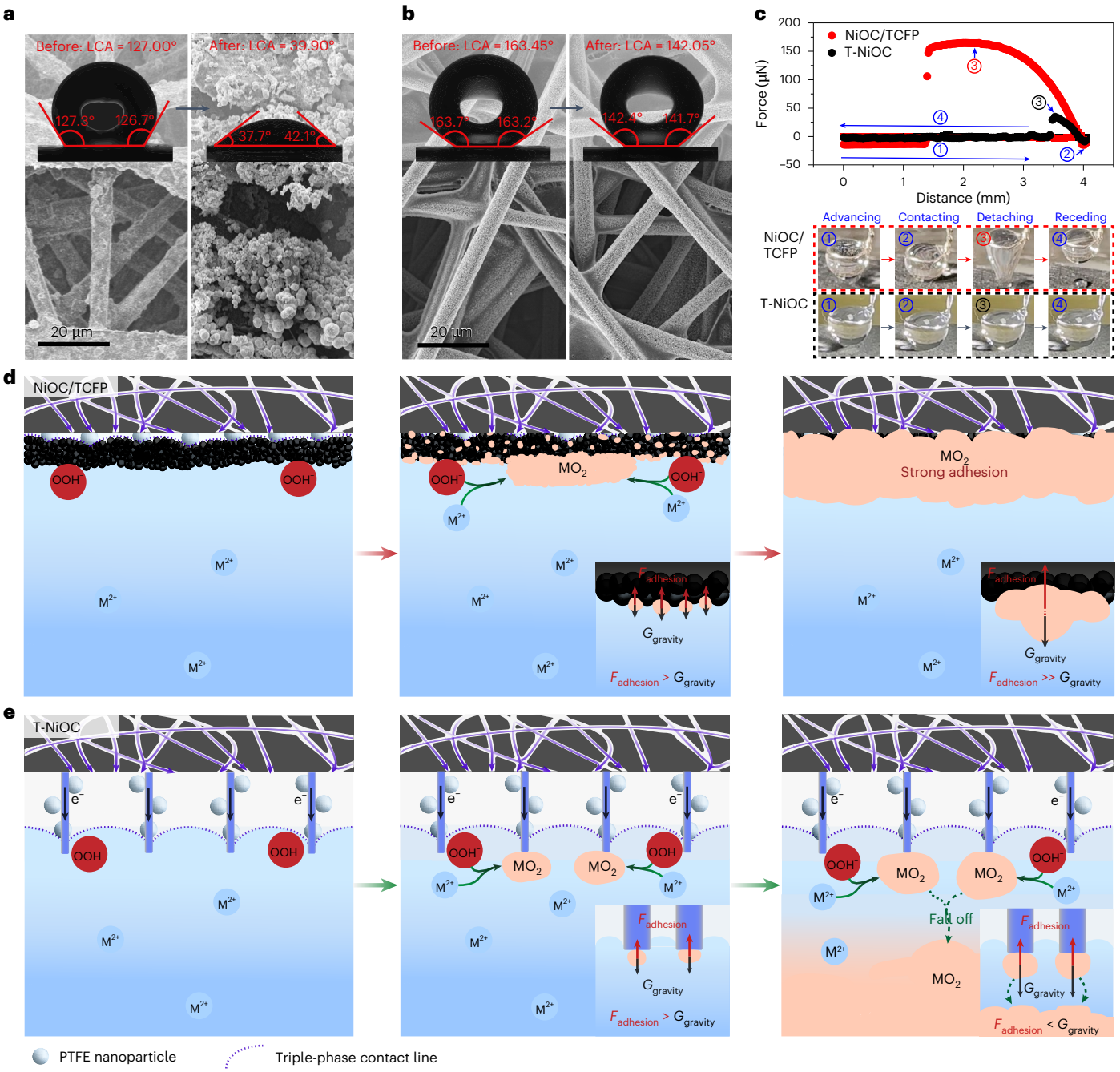

Fig. 4 | Self-cleaning mechanism of the T-NiOC electrode. a,**b**, The SEM images and LCAs of NiOC/TCFP (**a**) and T-NiOC (**b**) electrodes before and after 1 h reaction, respectively. **c**, Adhesive force and the corresponding optical images of T-NiOC and NiOC/TCFP. **d**,**e**, Schematic illustrations of the nucleation, growth and desorption/adhesion process of MO_2 on NiOC/TCFP (**d**) and T-NiOC (**e**) electrode surfaces, respectively; the insets are the corresponding stress analysis of MO_2 products on the electrode surface. $F_{adhesion}$ denotes the adhesion force between the electrode surface and the solid product, and $G_{gravity}$ denotes the gravity of the solid product itself.

electrode plays a crucial role in the in situ electrochemical synthesis of MO_2 (Supplementary Figs. 29–36). Insufficient polytetrafluoroethylene (PTFE) modification resulted in inadequate triple-phase contact lines (Supplementary Figs. 37–39) and reduced current density, while excessive modification increased resistance and impeded electron transfer[31] (Supplementary Fig. 40).

Indeed, the continuous synthesis of MO_2 heavily relies on the nucleation and growth processes. Compared with homogeneous nucleation, heterogeneous nucleation usually needs a lower nucleation barrier and facilitates easier initiation[32,33] (Supplementary Fig. 41). In this case, the elevated concentration of reactants (HO_2^-) at the electrode surface promoted the adherence of MO_2 and facilitated heterogeneous nucleation. According to the aforementioned characterizations, we hypothesize that, for NiOC/TCFP, the infiltration of electrolyte into the catalyst layer triggers the nucleation and growth of MO_2 products, occurring both within and on the surface of the NiOC/TCFP electrode, as depicted in Fig. 4d. The nucleus progressively expanded and covered the catalytic active sites because of the strong adhesion force induced by extensive contact area (inset of Fig. 4d), which swiftly hazarded the electrochemical synthesis of MO_2. In sharp contrast, the T-NiOC electrode with micro-/nanostructured surface morphology and hydrophobic chemical modification observably reduced solid–liquid contact

https://doi.org/10.1038/s41565-024-01815-x

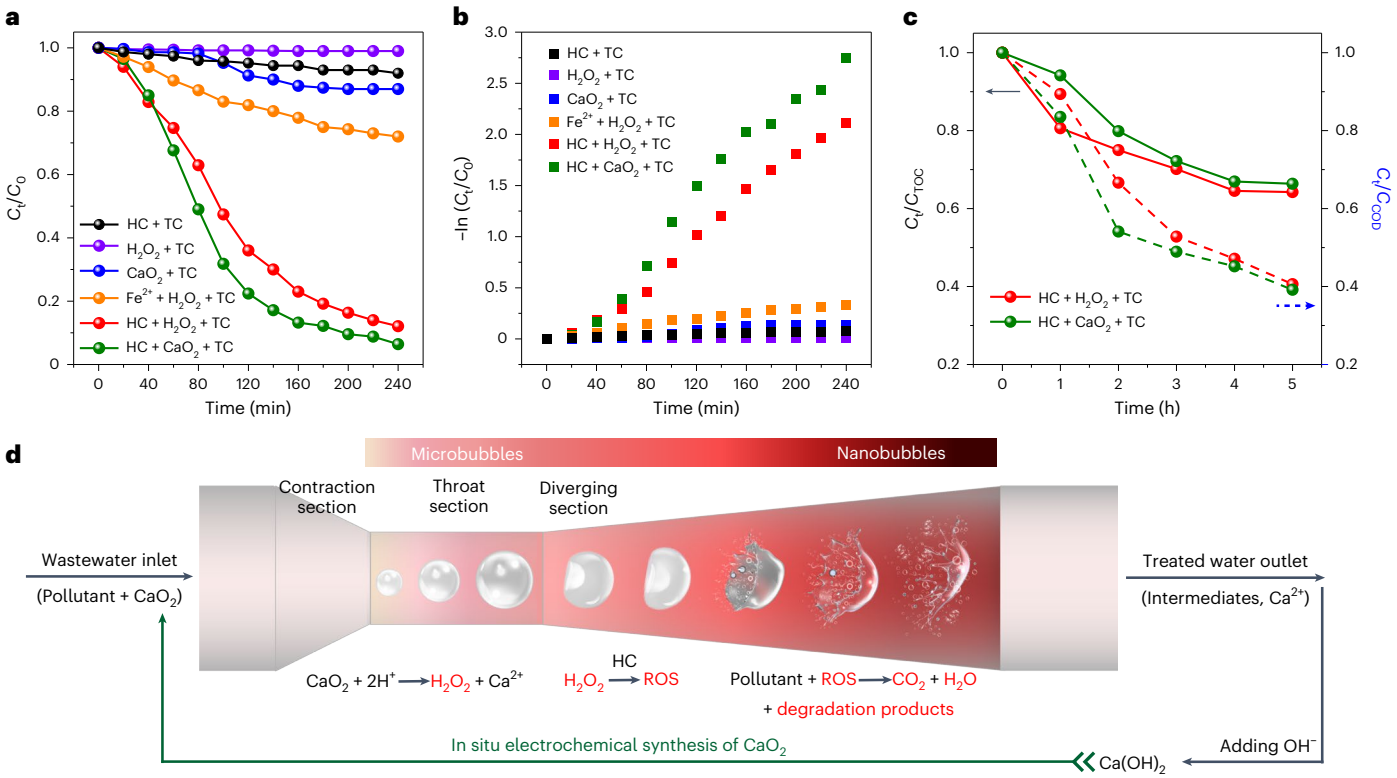

Fig. 5 | Degradation performance of as-synthesized CaO_2 and H_2O_2 with HC. **a**,**b**, Comparison of TC degradation efficiency (**a**) and kinetics (**b**) in different conditions. C_0 represents the initial concentration of TC and C_t is the remaining concentration of TC at a different time. **c**, The removal performance of COD and TOC in the HC + CaO_2/H_2O_2 + TC systems. C_{TOC} and C_{COD} represent the TC concentration measured by the TOC and COD methods, respectively. **d**, Mechanism diagram of pollutant degradation by HC + CaO_2.

area and impeded electrolyte penetration[34–38] (Fig. 4e). In addition, the micro-/nanostructured configuration enabled to trap and retain gas, establishing a robust gas barrier[39,40]. Thus, despite the fact that nucleation of MO_2 on the electrode remained predominantly heterogeneous, its weakened adhesion generated by needle-like morphology of MO_2 resulted in the detachment of smaller-sized MO_2 particles during the growth process (Supplementary Figs. 42 and 43 and Supplementary Video 1).

Compared with H_2O_2, MO_2 (especially CaO_2) usually exhibits superior chemical stability, which greatly reduces the risks of explosion and decomposition in terms of active O_2^{2-} (refs. 41,42). However, it is always questionable whether CaO_2 has similar oxidation properties to H_2O_2. Here the degradation performances of CaO_2 and H_2O_2 for tetracycline (TC) were examined with the assistance of HC (Supplementary Fig. 44). The microbubbles are transformed into nanobubbles through the instantaneous thermal effect induced by HC, and the enormous energy released during the rupture of nanobubbles cavity can effectively activate oxidants[43]. Figure 5a illustrates the degradation efficiencies of TC under different conditions in an acidic environment (pH ≈ 3), where HC + H_2O_2 and HC + CaO_2 systems achieved similar degradation efficiency of 87.9% and 93.6% for TC in 240 min, respectively, which were approximately ~3.2 times higher than that of conventional Fenton reaction. Note that the degradation of pollutants is nearly unaffected without HC or oxidants. The kinetic study demonstrated that the degradation of TC in HC + H_2O_2 and HC + CaO_2 systems followed close pseudo-first-order kinetics, as depicted in Fig. 5b. The removal efficiencies of chemical oxygen demand (COD) and total organic carbon (TOC) in HC + H_2O_2 and HC + CaO_2 systems were also investigated, as shown in Fig. 5c. After a reaction time of 5 h, both HC + CaO_2 and HC + H_2O_2 systems exhibited similar trends in the removal ratio of COD (~35%) and TOC (~60%), respectively.

The degradation results clearly demonstrated that CaO_2 and H_2O_2 showed analogous treatment effects on pollutants with HC. Furthermore, the preliminary electron paramagnetic resonance (EPR) analysis also revealed similar composition of reactive oxygen species (·OH and $\cdot O_2^{2-}$) generated in both systems (Supplementary Fig. 45). Moreover, owing to the enhanced solubility of CaO_2 in an acidic environment compared with neutral and alkaline conditions (Supplementary Fig. 46), we propose that it is initially converted to H_2O_2, which can be subsequently activated by HC to degrade TC in the CaO_2 + HC system, as schemed in Fig. 5d and Supplementary Fig. 47. After treatment, the neutralize step for the treated wastewater will precipitate Ca^{2+} as $Ca(OH)_2$, which is the raw materials for the in situ electrochemical synthesis of CaO_2 for the next O_2^{2-} cycle. To sum up, the utilization of CaO_2 as a reservoir for O_2^{2-} instead of H_2O_2 in environmental applications appears to be a feasible prospect for future advancements.

Conclusion

In summary, we have constructed an innovative and highly effective reaction system that enables the in situ conversion of high-concentration H_2O_2 generated by 2e⁻ ORR at the cathode surface into MO_2, thereby avoiding economic losses and safety risks associated with H_2O_2 enrichment. The continuous and high-rate production of MO_2 is highly dependent on the construction of the self-cleaning cathode with low adhesion force, which enables the separation of solid products from the reaction system without necessitating additional purification steps. In terms of current density (50 mA cm^{-2}), accumulated FE (~99%) and stability (>1,000 h), the proposed system exhibits unique superiority in practical applications. Moreover, the as-synthesized MO_2 was demonstrated with comparable performance to H_2O_2 in terms of pollutant degradation under HC conditions. Besides the highly efficient in situ electrochemical synthesis of MO_2,

this electrode design is generic and can definitely revolutionize other electrochemical solid-state synthesis reactions.

Online content

Any methods, additional references, Nature Portfolio reporting summaries, source data, extended data, supplementary information, acknowledgements, peer review information; details of author contributions and competing interests; and statements of data and code availability are available at https://doi.org/10.1038/s41565-024-01815-x.

References

1. Hu, H. et al. Chemoreactive nanotherapeutics by metal peroxide based nanomedicine. *Adv. Sci.* **8**, 2000494 (2021).
2. Wang, L.-H. et al. An inverse-breathing encapsulation system for cell delivery. *Sci. Adv.* **7**, eabd5835 (2021).
3. Yuan, X. et al. Self-triggered thermoelectric nanoheterojunction for cancer catalytic and immunotherapy. *Nat. Commun.* **14**, 5140 (2023).
4. Zheng, M. et al. Attenuation of pharmaceutically active compounds in aqueous solution by UV/CaO_2 process: influencing factors, degradation mechanism and pathways. *Water Res.* **164**, 114922 (2019).
5. Zhang, M. et al. Calcium-overload-mediated tumor therapy by calcium peroxide nanoparticles. *Chem* **5**, 2171–2182 (2019).
6. Lu, S., Zhang, X. & Xue, Y. Application of calcium peroxide in water and soil treatment: a review. *J. Hazard. Mater.* **337**, 163–177 (2017).
7. Xu, Q. et al. Improving the treatment of waste activated sludge using calcium peroxide. *Water Res.* **187**, 116440 (2020).
8. Qian, Y., Zhou, X., Zhang, Y., Zhang, W. & Chen, J. Performance and properties of nanoscale calcium peroxide for toluene removal. *Chemosphere* **91**, 717–723 (2013).
9. Rastinfard, A., Nazarpak, M. H. & Moztarzadeh, F. Controlled chemical synthesis of CaO_2 particles coated with polyethylene glycol: characterization of crystallite size and oxygen release kinetics. *RSC Adv.* **8**, 91–101 (2018).
10. Shen, S. et al. Synthesis of CaO_2 nanocrystals and their spherical aggregates with uniform sizes for use as a biodegradable bacteriostatic agent. *Small* **15**, 1902118 (2019).
11. Khodaveisi, J. et al. Synthesis of calcium peroxide nanoparticles as an innovative reagent for in situ chemical oxidation. *J. Hazard. Mater.* **192**, 1437–1440 (2011).
12. Dan, M. et al. Strategies and challenges on selective electrochemical hydrogen peroxide production: catalyst and reaction medium design. *Chem. Catal.* **2**, 1919–1960 (2022).
13. Xia, C. et al. Confined local oxygen gas promotes electrochemical water oxidation to hydrogen peroxide. *Nat. Catal.* **3**, 125–134 (2020).
14. Xia, C., Kim, J. Y. & Wang, H. Recommended practice to report selectivity in electrochemical synthesis of H_2O_2. *Nat. Catal.* **3**, 605–607 (2020).
15. Xia, C., Xia, Y., Zhu, P., Fan, L. & Wang, H. Direct electrosynthesis of pure aqueous H_2O_2 solutions up to 20% by weight using a solid electrolyte. *Science* **366**, 226–231 (2019).
16. Shi, X. et al. Understanding activity trends in electrochemical water oxidation to form hydrogen peroxide. *Nat. Commun.* **8**, 701 (2017).
17. Zhang, Y. et al. Metastable hexagonal phase SnO_2 nanoribbons with active edge sites for efficient hydrogen peroxide electrosynthesis in neutral media. *Angew. Chem. Int. Ed.* **62**, e202218924 (2023).
18. Vol'Nov, I. Y. I. *Peroxides, Superoxides, and Ozonides of Alkali and Alkaline Earth Metals* (Plenum Press, 1966).
19. Jung, E. et al. Atomic-level tuning of Co–N–C catalyst for high-performance electrochemical H_2O_2 production. *Nat. Mater.* **19**, 436–442 (2020).
20. Lu, Z. et al. High-efficiency oxygen reduction to hydrogen peroxide catalysed by oxidized carbon materials. *Nat. Catal.* **1**, 156–162 (2018).
21. Perry, S. C. et al. Electrochemical synthesis of hydrogen peroxide from water and oxygen. *Nat. Rev. Chem.* **3**, 442–458 (2019).
22. Tang, J. et al. Selective hydrogen peroxide conversion tailored by surface, interface, and device engineering. *Joule* **5**, 1432–1461 (2021).
23. Zuo, K. et al. Ultrahigh resistance of hexagonal boron nitride to mineral scale formation. *Nat. Commun.* **13**, 4523 (2022).
24. Xu, W. et al. Fast and stable electrochemical production of H_2O_2 by electrode architecture engineering. *ACS Sustain. Chem. Eng.* **9**, 7120–7129 (2021).
25. Huang, H. et al. Triphase photocatalytic CO_2 reduction over silver-decorated titanium oxide at a gas–water boundary. *Angew. Chem. Int. Ed.* **61**, e202200802 (2022).
26. Lu, Z. et al. Superaerophilic carbon-nanotube-array electrode for high-performance oxygen reduction reaction. *Adv. Mater.* **28**, 7155–7161 (2016).
27. Zhang, Q. et al. Highly efficient electrosynthesis of hydrogen peroxide on a superhydrophobic three-phase interface by natural air diffusion. *Nat. Commun.* **11**, 1731 (2020).
28. Lai, Y. et al. Designing superhydrophobic porous nanostructures with tunable water adhesion. *Adv. Mater.* **21**, 3799–3803 (2009).
29. Lin, Z. et al. Atomic Co decorated free-standing graphene electrode assembly for efficient hydrogen peroxide production in acid. *Energy Environ. Sci.* **15**, 1172–1182 (2022).
30. Wang, S., Liu, K., Yao, X. & Jiang, L. Bioinspired surfaces with superwettability: new insight on theory, design, and applications. *Chem. Rev.* **115**, 8230–8293 (2015).
31. Xing, Z., Hu, L., Ripatti, D. S., Hu, X. & Feng, X. Enhancing carbon dioxide gas-diffusion electrolysis by creating a hydrophobic catalyst microenvironment. *Nat. Commun.* **12**, 136 (2021).
32. De Yoreo, J. J. et al. Crystallization by particle attachment in synthetic, biogenic, and geologic environments. *Science* **349**, aaa6760 (2015).
33. Wu, K.-J., Tse, E. C. M., Shang, C. & Guo, Z. Nucleation and growth in solution synthesis of nanostructures—from fundamentals to advanced applications. *Prog. Mater. Sci.* **123**, 100821 (2022).
34. Newby, B.-m. Z., Chaudhury, M. K. & Brown, H. R. Macroscopic evidence of the effect of interfacial slippage on adhesion. *Science* **269**, 1407–1409 (1995).
35. Cui, L. et al. An anti-electrowetting carbon film electrode with self-sustained aeration for industrial H_2O_2 electrosynthesis. *Energy Environ. Sci.* **17**, 1754–5692 (2024).
36. Dhyani, A. et al. Design and applications of surfaces that control the accretion of matter. *Science* **373**, eaba5010 (2021).
37. Tuteja, A. et al. Designing superoleophobic surfaces. *Science* **318**, 1618–1622 (2007).
38. Golovin, K., Dhyani, A., Thouless, M. D. & Tuteja, A. Low–interfacial toughness materials for effective large-scale deicing. *Science* **364**, 371–375 (2019).
39. Chen, Y. et al. Bioinspired superhydrophobic surfaces, inhibiting or promoting microbial contamination? *Mater. Today* **67**, 468–494 (2023).
40. Wang, Y. et al. Water spider-inspired nanofiber coating with sustainable scale repellency via air-replenishing strategy. *Adv. Mater.* **35**, 2209796 (2023).
41. Chen, Z. et al. Enhancement of waste activated sludge dewaterability using calcium peroxide pre-oxidation and chemical re-flocculation. *Water Res.* **103**, 170–181 (2016).
42. Ma, Y., Zhang, B.-T., Zhao, L., Guo, G. & Lin, J.-M. Study on the generation mechanism of reactive oxygen species on calcium peroxide by chemiluminescence and UV-visible spectra. *Luminescence* **22**, 575–580 (2007).
43. Gao, Y., Li, M., Sun, C. & Zhang, X. Microbubble-enhanced water activation by cold plasma. *Chem. Eng. J.* **446**, 137318 (2022).

Methods

Chemicals and materials

Reagents including NaOH (≥97%), $Ba(OH)_2{\cdot}8H_2O$ (≥98%), $Ca(OH)_2$ (≥95%), $C_{22}H_{24}N_2O_8{\cdot}HCl$ (TC) PTFE preparation (60 wt%), Nafion-117 solution (~5% in a mixture of lower aliphatic alcohols and water), 5,5-dimethyl-1-pyrroline-*N*-oxide (DMPO), polyethylene oxide (M_v ~10,000) and C_2H_6OS (DMSO) were procured from Shanghai Aladdin Bio-Chem Technology. $Ni(NO_3)_2{\cdot}6H_2O$, $CO(NH_2)_2$, H_2SO_4, HCl (36%), H_2O_2 (30 wt%), BaO_2 (≥99%), TC ($C_{22}H_{24}N_2O_8$) and methanol were procured from Sinopharm Chemical Reagent. Carbon fibre paper (CFP; TGP-H-060, 0.19 mm) and TCFP (TGP-H-060-10 wt%, 0.19 mm) were purchased from TORAY Industries. $Ti(SO_4)_2$ and $Sr(OH)_2{\cdot}8H_2O$ (≥99.5%) were procured from Macklin. SrO_2 (≥98%) and CaO_2 (≥75%) were procured from Sigma-Aldrich. All chemicals were used as received without further purification.

Synthesis of the T-NiOC electrode

The synthesis of the T-NiOC electrode involves a solvothermal method, carbonization and PTFE coating via a hydrothermal method. The $Ni(OH)_2$ array was fabricated on CFP using the solvothermal method with methanol as the solvent, following a methodology previously reported by our research group[24]. Initially, 1 mmol of $Ni(NO_3)_2{\cdot}6H_2O$ and 10 mmol of $CO(NH_2)_2$ were dissolved in 36 ml of methanol solution and vigorously stirred to achieve homogeneity. Subsequently, both the solution and the prepared CFP (2 × 3 cm^2), which had been cleaned by a plasma machine for 10 min, were transferred to a 50 ml Teflon-lined stainless-steel autoclave. The temperature was maintained at 120 °C for 12 h. After naturally cooling to room temperature, $Ni(OH)_2$@CFP can be obtained by undergoing ultrasonic cleaning with distilled water and ethanol for 5 min, and then dried. Subsequently, $Ni(OH)_2$@CFP was placed on a porcelain boat containing 2 g of polyethylene oxide and carbonized at an argon flow rate of 20 sccm and a heating rate of 10 °C min^{-1}, and the temperature was maintained at 800 °C for 2 h. The NiOC electrode was fabricated.

The as-prepared NiOC electrode was placed in an autoclave containing 40 ml of a 10 wt% PTFE solution and heated at 100 °C for 30 min. After natural cooling to room temperature and subsequent drying at 60 °C, the electrode underwent heat treatment in an air atmosphere at 350 °C for 30 min. Finally, the T-NiOC electrode was fabricated.

Synthesis of the NiOC/TCFP electrode

NiOC/TCFP electrodes can be fabricated by the drop-coating NiOC catalyst (~3 mg cm^{-2}) on TCFP (10 wt% PTFE).

Synthesis of SrO_2 using the chemical method

Different volumes of the highly concentrated H_2O_2 (30 wt%) were added to the saturated $Sr(OH)_2$ solutions (50 ml), and the corresponding products were collected after 1 h of reaction.

Calculation of the utilization rate of H_2O_2 in the chemical synthesis of MO_2

$$\text{Utilization ratio}(\%) = \frac{m_{\text{real}}}{m_{\text{theory}}} \times 100 = \frac{m_{\text{real}}}{\frac{\omega \times \rho_{H_2O_2} \times V \times 1{,}000 \times M_{MO_2}}{M_{H_2O_2}}} \times 100\% \quad (1)$$

where M_{MO_2} and $M_{H_2O_2}$ represent the relative molecular weights of MO_2 and H_2O_2, respectively; ρ represents the density of H_2O_2 (ρ = 1.122 g l^{-1}); ω is the concentration of H_2O_2 (wt%); and V is the volume of H_2O_2 (l). m_{real} represents the mass of the MO_2 product obtained experimentally, and m_{theory} represents the mass of the MO_2 product obtained theoretically.

Characterization

The XRD patterns of the catalysts and products were recorded by D8 ADVANCE DAVINCI (Bruker). SEM images were obtained by S4800 (Hitachi) operating at a voltage of 10 kV. Transmission electron microscopy images were acquired using the Tecnai F20 electron microscope (FEI) with an acceleration voltage of 200 kV. X-ray photoelectron spectroscopy was measured using Axis Ultra DLD (Kratos). TGA was conducted under a nitrogen atmosphere using the TG209F1 (Netzsch). TOC was measured using multi N/C 3100 (Jena). EPR measurements were conducted using a Bruker E500 EPR spectrometer.

Surface wetting properties characterization

LCA and SA. The optical contact angle and surface/interfacial tension measurement system (OSA 60G, LAUDA Scientific) was used for measuring the LCA and sliding angle (SA) between the electrolyte and the electrode. The electrolyte (~50 µl) was drop-casted on the electrode surface under ambient conditions at room temperature, and then the LCA was measured. In addition, a rotating platform was utilized to measure the SA.

Adhesive force. The interaction force between the electrolyte and electrode interface was assessed utilizing a high-sensitivity microelectromechanical balance system (Data Physics DCAT11). A drop of electrolyte (0.4 M NaOH + saturated $Sr(OH)_2$, ~20 µl) was suspended on a pristine Pt ring (d = 5 mm), and the initial force was calibrated to zero.

Purity determination of MO_2 through TGA. TGA was conducted under a nitrogen atmosphere using the TG209F1 (Netzsch). The temperature ranged from room temperature to the decomposition temperature at a rate of 10 °C min^{-1}. The decomposition products of MO_2 are MO and O_2, which can be represented by chemical equation (equation (2)):

$$2MO_2 \rightarrow 2MO + O_2 \uparrow \quad (2)$$

The weight loss observed during the thermogravimetric process corresponds to the amount of oxygen released, thereby enabling determination of MO_2 purity (chemical pure (CP)) based on the stoichiometry of the decomposition reaction (equation (3)):

$$\begin{aligned} \text{CP}(\%) &= \frac{\Delta m_{O_2}}{m_0} \times \frac{M_{MO_2}}{\frac{1}{2} \times M_{O_2}} \times 100 = \frac{\Delta\text{TG} \times m_0}{m_0} \times \frac{M_{MO_2}}{\frac{1}{2} \times M_{O_2}} \\ &= 2\Delta\text{TG} \times \frac{M_{MO_2}}{M_{O_2}} \end{aligned} \quad (3)$$

where M_{MO_2} and M_{O_2} represent the relative molecular weights of MO_2 and O_2, respectively. The mass loss of O_2 (Δm_{O_2}) can be expressed as $\Delta m_{O_2} = \Delta\text{TG} \times m_0$, where ΔTG represents the percentage of oxygen lost in the TGA and m_0 refers to the initial weight.

Electrochemical measurements. The electrochemical tests were conducted at room temperature using the CHI 760E (Chenhua Instrument 760E) workstation. In a typical three-electrode system, graphite rod and Hg/HgO (1 M KOH) electrode were used as the counter and reference electrodes, respectively. The electrode (T-NiOC or NiOC/TCFP, ~1 cm^2) was used as the working electrode. During all the electrochemical measurements, a continuous supply of oxygen was essential to sustain the rapid rate of oxygen consumption. All samples were pre-stabilized through cyclic voltammetry for ~20 cycles to achieve a stable current density, and the linear sweep voltammetry measurements were conducted in 0.4 M NaOH + saturated $Sr(OH)_2$ electrolytes at a scan rate of 5 mV s^{-1}. The long-term stability test utilized a two-electrode system with a constant current density of 50 mA cm^{-2}, incorporating a DSA (4 cm^2) as the counter electrode and using the as-prepared electrode (T-NiOC or NiOC/TCFP) as the working electrode. The electrolyte was 0.4 M NaOH + saturated $Sr(OH)_2$ solution.

Determination of H_2O_2 concentration. During the assessment of H_2O_2 selectivity, the concentration of H_2O_2 produced by the working

electrode measurement was collected using a two-compartment system separated by Nafion-117. The two chambers (cathode and anode compartment) were both filled with 15 ml of the identical electrolyte solution. The H_2O_2 concentration was determined using a conventional titration method, in which titanium (IV) sulfate ($Ti(SO_4)_2$) reacts with H_2O_2 to form a stable yellow-orange titanium (IV)-peroxide complex. The intensity of this complex increases proportionally with the concentration of H_2O_2.

By using UV–vis spectroscopy to measure the wavelength of titanium (IV)-peroxide complex at 408 nm, the corresponding H_2O_2 concentration can be determined. In detail, the 2 ml $Ti(SO_4)_2$ solution (which dissolves 2 mmol l^{-1} $Ti(SO_4)_2$ in a 2 M H_2SO_4 solution) was thoroughly mixed with an equal volume of the sample for testing. The standard curve (Supplementary Fig. 15) was established by quantifying known concentrations of H_2O_2 using UV–vis spectroscopy.

The theoretical amount of H_2O_2 in 15 ml solution can be determined by quantifying the charge consumed during the two-electron oxygen reduction process. The equation is expressed as follows (equation (4)):

$$\mathrm{FE}_{\mathrm{H_2O_2}}(\%) = \frac{n\times F\times c\times V}{I_{\mathrm{total}}\times t} = \frac{2\times 96{,}485\left(\mathrm{C\,mol^{-1}}\right)\times c_{\mathrm{H_2O_2}}\left(\mathrm{mol\,l^{-1}}\right)\times V(\mathrm{l})}{I_{\mathrm{total}}\,(\mathrm{A})\times t\,(\mathrm{s})} \quad (4)$$

where n represents the number of electrons transferred ($n = 2$), F is the Faraday constant (96,485 C mol^{-1}), c is the concentration of H_2O_2 (mol l^{-1}), V is the volume of electrolyte (l), I_{total} is the total operated current (A) and t is the operated time (s).

Utilization of HC for degradation

HC reactor set-up. The homemade HC set-up consists of a pump (with a flow rate of 13 l min^{-1}, a maximum outlet pressure of 20 MPa and a power of 5.5 kW), control valves, pressure gauges, fluid flowmeter, cavitation generating unit, storage tank, refrigerator and connecting pipe. The pump connects the main line and bypass line, conveying the solution from the storage tank to the circulation system. The bypass line is used to regulate the inlet pressure of the main line, while the pressure gauge and flowmeter are utilized for measuring respective pressures and flows in the main line. All components of the pump body are constructed using 304 stainless steel.

Degradation using combination of HC and CaO_2/H_2O_2. A solution of CaO_2 or H_2O_2 was reconstituted with a concentration of 0.8 mol l^{-1} in an HCl (pH = 3) solution, followed by the addition of 10 mg l^{-1} TC. The solution was introduced into the storage tank while adjusting the reaction temperature to 25 °C and setting the inlet pressure at 0.5 MPa, followed by initiating the reaction apparatus. The TC concentration in the solution was sampled at 20 min intervals, and the COD in the system was determined through acid potassium dichromate titration.

EPR technique is utilized for detecting free radicals. The spin trap DMPO is utilized for the detection of $\cdot O_2^{2-}$ and ·OH in DMSO and water, respectively, within hydraulic HC + CaO_2 and HC + H_2O_2 systems. Typically, 5 µl DMPO and 0.5 ml solution (after HC + CaO_2/H_2O_2 activation) were added to 10 ml of deionized water (for ·OH detection) or methanol (for $\cdot O_2^{2-}$ detection).

Estimating the distribution of HO_2^- concentration on the electrode surface. The rotating ring-disk electrode is used as a model electrode to monitor the concentration of H_2O_2 produced and accumulated on the disk as well as diffusive concentration on the ring. We assume that the diffusion of H_2O_2 from the disk to ring is in accordance with Fick's first law owing to the close proximity of the disk to ring and the static electrolyte[44].

According to Fick's diffusion law, the diffusion flux (J, mol cm^{-2} s^{-1}) across a unit cross-sectional area perpendicular to the direction of diffusion in a unit of time is directly proportional to the concentration gradient at that specific cross section[45]. The flux of H_2O_2 ($J_{H_2O_2}$) flowing through a distance (x) can be expressed as equation (5):

$$J_{\mathrm{H_2O_2}} = D_{\mathrm{H_2O_2}} \times \frac{\mathrm{d}c_{\mathrm{H_2O_2}}}{\mathrm{d}x} \quad (5)$$

where $J_{H_2O_2}$ (mol cm^{-2} s^{-1}) is the diffusion flux of H_2O_2, $D_{H_2O_2}$ (cm^2 s^{-1}) is the diffusion coefficient of H_2O_2 and x (cm) is the diffusion distance, respectively.

Since the distance from the disk to ring is short enough (0.032 cm), equation (5) can be simplified as equation (6):

$$J_{\mathrm{H_2O_2}} = D_{\mathrm{H_2O_2}} \times \frac{\mathrm{d}c_{\mathrm{H_2O_2}}}{\mathrm{d}x} = D_{\mathrm{H_2O_2}} \times \frac{c^s_{\mathrm{H_2O_2}} - c^x_{\mathrm{H_2O_2}}}{x} \quad (6)$$

where $c^s_{H_2O_2}$ (mol cm^{-3}) is the concentration of H_2O_2 at the electrode surface and $c^x_{H_2O_2}$ is the concentration of H_2O_2 at position x, respectively.

Since the in situ-generated H_2O_2 on the disk surface follows the chemical reaction equation (equation (7)), the relationship between current (I_{disk}) and the H_2O_2 concentration ($c^s_{H_2O_2}$) follows Faraday's law[46] and can be expressed as equation (8):

$$\mathrm{O_2} + 2\mathrm{H_2O} = 2\mathrm{H_2O_2} \quad (7)$$

$$I_{\mathrm{disk}} = \frac{nF}{\upsilon_i} \times J_{\mathrm{H_2O_2}} = \frac{nF}{\upsilon_i} \times D_{\mathrm{H_2O_2}} \times \frac{c^s_{\mathrm{H_2O_2}} - c^x_{\mathrm{H_2O_2}}}{x} \quad (8)$$

where I_{disk} is the current density of the disk, n is the electron transfer number, F is the Faraday constant and υ_i is the stoichiometric number of H_2O_2, respectively.

COMSOL simulation of the distribution of HO_2^- concentration on the electrode surface. The distribution of ion concentration at any given time can be determined by analysing the ion transport properties in solution and the ion generation rate on the electrode surface. Given the stationary nature of the solution, ions can accumulate at an exceptionally high concentration on the electrode surface. Consequently, accurately accounting for the ion diffusion coefficient as a function of concentration, $D(c)$, and appropriately adjusting the parameters within $D(c)$ are crucial to ensure that reasonable outcomes are obtained.

The solution domain of the equation is a one-dimensional space, where one side represents the electrode surface and the other side represents an open boundary positioned sufficiently far from the electrode. The concentration of ions (c_i) satisfies the convection–diffusion equation (equation (9)):

$$\frac{\partial c_i}{\partial t} - \nabla \times (D_i \times \nabla c_i) = R \quad (9)$$

where R is the source item, with $R = R(J)$ being a known function on the electrode side. The isotropic diffusion coefficient of the ion is denoted as D_i (equation (10)), and subsequent modifications have been implemented for $i \in \{HO_2^-,\ OH^-\}$:

$$D_i = \begin{cases} D_{i0}, & c_i \le c_{i1} \\ D_{i0}\left(\frac{c_i}{c_{i1}}\right)^{-6}, & c_{i2} \ge c_i > c_{i1} \\ D_{i0}\left(\left(\frac{c_i}{c_{i1}}\right)^{-6} + \left(\frac{c_i}{c_{i2}}\right)^{-36}\right), & c_i > c_{i2} \end{cases} \quad (10)$$

For the static fluid (equation (11)),

$$D_i \times \nabla c_i = 0 \quad (11)$$

The initial concentration of HO_2^- in the entire computing domain is zero.

Data availability

All experimental data are available in the main text or the supplementary materials.

References

44. Liu, X. & Koper, M. T. M. Tuning the interfacial reaction environment for CO_2 electroreduction to CO in mildly acidic media. *J. Am. Chem. Soc.* **146**, 5242–5251 (2024).
45. Fick, A. V. On liquid diffusion. *Lond. Edinb. Dublin Philos. Mag. J. Sci.* **10**, 30–39 (1855).
46. Resta, R. Faraday law, oxidation numbers, and ionic conductivity: the role of topology. *J. Chem. Phys.* **155**, 244503 (2021).

Acknowledgements

This work was supported by the National Natural Science Foundation of China (22379154 and 22105214), the Ningbo Yongjiang Talent Introduction Programme (2021A-036-B), the Ningbo S&T Innovation 2025 Major Special Program (2022Z205), the Bellwethers Project of Zhejiang Research and Development Plan (2022C01158) and the National Science Foundation of Ningbo (2022J296).

Author contributions

Z.L. and J.J. supervised the project. M.W. and W.X. synthesized the electrodes and conducted the materials characterization and corresponding data processing. M.W., W.Z. and Y.W. designed the schemes. W.G. provided the COMSOL simulation. J.C., D.Z. and J.J. conducted the pollutant degradation component. M.W., W.X. and Z.L. wrote the paper. All authors discussed and contributed to the work.

Competing interests

The authors declare no competing interests.

Additional information

Supplementary information The online version contains supplementary material available at https://doi.org/10.1038/s41565-024-01815-x.

Correspondence and requests for materials should be addressed to Wenwen Xu, Jinping Jia or Zhiyi Lu.

Peer review information *Nature Nanotechnology* thanks Deli Wang and the other, anonymous, reviewer(s) for their contribution to the peer review of this work.